Article:

Alsharif, A., Moinuddin, S.Q. and Pinna, C. (2026) Small punch testing and scanning electron microscopy analysis of damage evolution in dual-phase steel. Scientific Reports. ISSN: 2045-2322

https://doi.org/10.1038/s41598-026-40489-4

Scientific Reports

https://doi.org/10.1038/s41598-026-40489-4

Article in Press

Small punch testing and scanning electron microscopy analysis of damage evolution in dual-phase steel

Received: 26 November 2025

Accepted: 13 February 2026

Published online: 17 February 2026

Cite this article as: Alsharif A., Moinuddin S.Q. & Pinna C. Small punch testing and scanning electron microscopy analysis of damage evolution in dual-phase steel. *Sci Rep* (2026). https://doi.org/10.1038/s41598-026-40489-4

Asim Alsharif, Syed Quadir Moinuddin & Christophe Pinna

We are providing an unedited version of this manuscript to give early access to its findings. Before final publication, the manuscript will undergo further editing. Please note there may be errors present which affect the content, and all legal disclaimers apply.

If this paper is publishing under a Transparent Peer Review model then Peer Review reports will publish with the final article.

ARTICLE IN PRESS

© The Author(s) 2026. **Open Access** This article is licensed under a Creative Commons Attribution-NonCommercial-NoDerivatives 4.0 International License, which permits any non-commercial use, sharing, distribution and reproduction in any medium or format, as long as you give appropriate credit to the original author(s) and the source, provide a link to the Creative Commons licence, and indicate if you modified the licensed material. You do not have permission under this licence to share adapted material derived from this article or parts of it. The images or other third party material in this article are included in the article's Creative Commons licence, unless indicated otherwise in a credit line to the material. If material is not included in the article's Creative Commons licence and your intended use is not permitted by statutory regulation or exceeds the permitted use, you will need to obtain permission directly from the copyright holder. To view a copy of this licence, visit http://creativecommons.org/licenses/by-nc-nd/4.0/.

Small Punch Testing and Scanning Electron Microscopy Analysis of Damage Evolution in Dual-Phase Steel

Asim Alsharif [1]*, Syed Quadir Moinuddin[2], Christophe Pinna[3]
[1] Department of Mechanical Engineering, College of Engineering in Yanbu, Taibah University, Yanbu Al-Bahr, 46425, Saudi Arabia
[2] Department of Mechanical Engineering, College of Engineering, King Faisal University, Al-Ahsa-31982, Saudi Arabia.
[3] Department of Mechanical Engineering, The University of Sheffield, Mappin Street, S13JD Sheffield, UK.

*Corresponding author: aasharif@taibahu.edu.sa

Abstract

Dual-phase (DP) steels are widely used in the automotive industry due to their excellent balance of strength and ductility. Enhancing their formability and crash performance requires a deeper understanding of microstructural deformation and damage mechanisms. This study presents an in-depth micromechanical investigation of damage initiation and propagation in DP1000 steel using a novel small-punch (SP) test setup combined with three-dimensional digital image correlation (3D DIC) and scanning electron microscopy (SEM). The test was strategically interrupted at multiple stages to capture the evolution of cracking. Initial cracks appeared at a punch displacement of approximately 1.12 mm, while the final stages revealed microstructural crack propagation resulting from deformation localized near the ferrite (F) – martensite (M) interface, leading to cracking of adjacent M islands or void growth within the F. 3D DIC measurements revealed maximum principal surface strains up to 23% before cracking. SEM analysis confirmed that the dominant through-thickness crack initiated at the punch sample interface and propagated toward the upper surface, aligning with surface strain localizations. M cracking was limited to the early stages, while subsequent damage growth was F-dominated. This integrated experimental approach offers new insights into the phase-specific damage behaviour and supports the development of predictive models for the formability and failure of advanced high-strength steels.

Keywords: Dual Phase (DP 1000) Steel, SP Test (biaxial loading), Microstructure Damage and Modelling, Crack initiation and propagation, Scanning Electron Microscope, Digital Image Correlation.

1. Introduction

Forming operations are widely used in the automotive industry to produce high-quality car body parts, with complex loads shaping the final geometry [1]. The increasing use of advanced high-strength steels (AHSS) to reduce vehicle weight requires an accurate prediction of material behaviour and ductility during forming [2-4]. Formability, defined as a material's ability to undergo plastic deformation without defects such as necking, wrinkling, or cracking, is a critical design parameter [5]. To quantify formability, various experimental techniques have been developed, particularly those replicating complex multiaxial stress states encountered during forming operations. While uniaxial tensile tests provide baseline mechanical properties, they cannot capture multiaxial stress states typical of real forming processes. To address this, Forming Limit Diagrams (FLDs) are employed, plotting true major versus minor strain to delineate safe deformation limits [6]. The Forming Limit Curve (FLC) identifies strain combinations leading to necking or fracture, with experimental determination often performed using optical methods such as DIC. Standardized procedures (e.g., BS EN ISO 12004-2:2008 [6]) ensure reproducibility and support predictive modelling for metal forming and alloy design.

Various experimental methods have been developed to evaluate sheet metal formability under different stress states. The Swift cup [5, 7], Fukui conical cup [5], and Limiting Dome Height (LDH) tests [5] assess drawability and biaxial stretching, while standardized ball-punch tests (e.g., E643-15, 2015) [8] provide reproducible measures of punch height at failure. More recently, research has increasingly focused on post-necking deformation and digital strain measurement. Mendes-Fonseca et al. [9] recently highlighted the relevance of bendability by comparing three-point and V-die bending in DP steels, demonstrating that different deformation modes trigger distinct failure mechanisms. Paul et al. [10] demonstrated that DIC-based reconstruction significantly improves post-necking stress–strain characterization in steels, while Paul [11] showed that microstructure and deformation mechanisms strongly influence the FLC in automotive alloys. Paul [12] further reviewed key controlling factors for FLC, highlighting phase morphology, strain partitioning, and heterogeneity, whereas Paul [13] emphasized the importance of edge-crack sensitivity and phase distribution in stretch-flange formability, directly relevant to dual-phase steel damage behaviour. The SP test, a miniaturized variant integrated with 3D DIC, enables microstructural-scale assessment of deformation and damage, using specimens of smaller diameter than conventional tests [8, 14]. SP tests, combined with finite element (FE) modelling [15], have demonstrated strong correlations with uniaxial tensile tests [16-18], and can also estimate fracture toughness [19-21].

In DP steels, the SP test effectively captures microstructural damage mechanisms, including localized strain hardening, void nucleation, and crack evolution at F–M interfaces [22-36]. Peng et al. [25] introduced a stress–strain reconstruction model based on SP test data to predict the tensile behavior and fracture resistance of DP600, while Rodríguez et al. [22] combined SP test with modelling to estimate fracture parameters in ductile steels. A significant body of work has further explored crack initiation and propagation mechanisms in DP steels, underscoring the critical role of microstructural heterogeneity [24, 26-29, 37]. For example, in DP1000, Alsharif, et al. [30], Alharbi et al. [31] and Ghadbeigi et al. [32] identified M rupture as a dominant damage initiation mechanism. Soyarslan et al. [33] reported surface crack initiation in DP1000 sheets, describing propagation using Gurson’s criterion, while Rèche et al. [34] observed similar surface-driven crack initiation in transformation-induced plasticity (TRIP) steels. Wang and Wei [35] showed that cracks tend to propagate along F–M interfaces or through the M phase, and Uthaisangsuk et al [36]. demonstrated that rupture strains in DP600 can be accurately assessed except under biaxial strain paths. Avramovic-Cingara et al. [32] showed that in DP600, M microcracks can initiate at very low strains (~0.029), after which void nucleation at F–M interfaces (~0.09) becomes the dominant damage mechanism, followed by interface decohesion and void growth along F ligaments, including occasional large voids at inclusions. Their related study on DP600-B [33] similarly observed M cracking (~13% strain), interfacial decohesion, and final void coalescence. Saeidi et al. [19] reported that in DP780, voids primarily nucleate at F-F-M triple junctions and narrow F regions between M islands, consistent with [34], occurring continuously up to fracture, with faster void growth under low stress triaxiality. Complementing these findings, Pelligra et al. [38] showed that vanadium alloying alters M strength and F-M constraint in DP1300, modifying microstrain partitioning and deformation pathways, and thereby influencing damage initiation, supporting the control of fracture behaviour by microstructural topology and composition.

Recent studies have highlighted M fracture as a dominant damage mechanism in DP1000 and DP600, with cracks often propagating along phase boundaries. In Tasan et al. [39], an experimental-simulation research study was carried out to examine stress and strain splitting in multiphase alloys, such as DP steels. Their results indicate that strain is concentrated mainly in the F phase during plastic deformation since it has a lower yield strength, whereas the M is the one that supports more stress. The simulations of crystal plasticity showed that the mechanical incompatibility at F-M interfaces is the source of this heterogeneous strain distribution. The paper notes that the deformation of DP steels is non-homogeneous in nature and highly dependent on the morphology of phases and local constraint. As a continuation of this study, Tasan et al. [40] also examined the strain localization and damage mechanisms in DP steels through coupled in-situ deformation experiments and crystal plasticity modelling. They noted that the localization of strain in F areas near M islands starts, which results in concentrations of stress at the phase boundaries. These localized areas of deformation serve as forerunners to damage initiation, especially the formation of voids at F-M interfaces. The article underlines that microstructural heterogeneity is strongly connected with deformation mechanisms in DP steels, but not only with the global loading conditions. Basu et al. [41] studied the microstructure–property relationship in DP steels, showing that refined M morphology and uniform phase distribution improve load transfer between F and M. Homogeneous strain distribution delays localization and enhances ductility. The study confirms that deformation mechanisms in DP steels can be tailored via microstructural parameters—particularly M size, shape, and distribution—and that excessive strain partitioning accelerates localization and damage, corroborating Tasan et al. [39, 40] findings on the role of strain incompatibility in failure. Basu et al. [42] studied the influence of microstructural size on micro-hole expansion and fracture toughness in DP steel sheets. They found that deformation-induced damage initiates via void nucleation in M or at F-M interfaces, progressing through void growth and coalescence. Micro-hole expansion strongly depends on M morphology and phase connectivity, linking fracture resistance directly to deformation processes. The study confirms that plastic deformation, strain localization, and damage evolution are closely interrelated, and optimizing microstructural features can delay localization, enhancing formability and fracture toughness. Deformation mechanisms may also vary with material type, temperature, and applied stress.

Despite advances in formability testing, the behaviour of DP1000 steels remains incompletely understood, particularly regarding local strain evolution, strain localization, and damage initiation under biaxial and constrained loading [25–27, 39]. Most tests provide global failure limits but do not capture the spatial and temporal evolution of strain fields at the microscale. Experimental studies using full-field techniques such as 3D DIC, especially when combined with post-deformation SEM analysis, are still limited. To address these gaps, this study presents an in-depth micromechanical investigation of damage initiation and propagation in DP1000 steel using a novel SP test methodology that integrates 3D DIC and SEM. The approach combines two complementary experiments: one interrupted SP test without DIC to directly observe crack initiation and early crack propagation on the top surface via SEM, and a second SP test with 3D DIC to quantify macroscopic strain localization during deformation, followed by post-mortem SEM examination of crack propagation through the specimen thickness. This SP–DIC–SEM strategy enables a direct correlation between macroscopic strain patterns and microstructural damage, providing novel insights into the mechanisms governing fracture and supporting the development of more physically informed formability models for advanced high-strength steels.

2. Experimentation

DP1000 steel was selected for investigation. It consists of two primary phases: (1) white martensite (M) islands embedded within (2) a dark ferrite (F) matrix [30]. The average ferrite grain size is approximately 4.2 µm, as determined using the line-intercept method in accordance with ASTM E112.The material was supplied as a 1.5 mm thick uncoated steel sheet, manufactured by Tata Steel (IJmuiden, Netherlands). The chemical composition provided by the manufacturer is presented in Table 1. The M phase accounts for approximately 51% of the total volume. It was produced by intercortical annealing conducted between the Ac_1 and Ac_3 temperatures, typically in the range of 790–800 °C. At this temperature, approximately half of the microstructure transformed into austenite, while the remaining phase consisted of F. During intercritical annealing, carbon preferentially partitioned into the austenite, resulting in its enrichment. Subsequent rapid quenching caused the austenite to transform into M, whereas the F phase was retained, yielding the characteristic F-M microstructure of DP1000 steel [43, 44]. For reference and for use in subsequent modelling, the key tensile properties of DP1000 derived from standard uniaxial tensile tests are summarized in Table 2. However, the full engineering stress–strain curve obtained from standard tensile testing is provided in Appendix A (See Fig. A1)

Table 1 Chemical composition weight ratio (wt%) of DP1000

Ni	Si	Mn	V	Cr	C	Nb
0.0325	0.473	1.522	0.012	0.0271	0.153	0.0135

Table 2 Tensile properties of DP 1000 steel

Tensile Properties	Yield Strength (MPa)	Ultimate Tensile Strength (MPa)	Elastic Modulus (GPa)	Poisson's Ratio (–)	Density (kg/mm³)	Elongation		
						Uniform (ε_u)	Total (ε_T)	Post Uniform (ε_{pu})
Value	662	1109	180	0.30	7.85×10^{-6}	0.06	0.11	0.05

2.1 SP Test Strategy and Configuration

The SP test was designed to enable a systematic correlation between macroscopic strain localization and microstructural damage evolution in DP1000 steel while remaining compatible with both 3D DIC measurements and SEM observations. Since continuous in-situ monitoring of microcrack initiation at the microstructural length scale is not feasible within the current experimental setup, the investigation was structured using two complementary SP tests, each targeting a specific length scale of deformation and damage. The first SP test was interrupted for SEM observation of crack initiation, while the second used 3D DIC to map strain localization, followed by post-mortem SEM to examine crack propagation. This strategy links macroscopic strain patterns with microstructural damage and fracture features.

To accommodate both experimental objectives, the SP test geometry and tooling were adapted to the University of Sheffield’s Lea Lab testing facilities while following established macro-punch testing principles. Although strict standard dimensions were not adopted due to equipment constraints, the design remains consistent with functional SP test configurations reported in the literature [40–42]. Circular specimens with a diameter of 30 mm and a thickness of 1.5 mm were selected, ensuring sufficient stiffness, repeatability, and compatibility with both DIC and SEM analysis.

2.1.1. Design of the top die, bottom die, and punch tool

The top-die dimensions directly influence the force–displacement response. A chamfer (flat or curved) can prevent specimen shearing [45],[46]. In this experiment, the top die is fastened to the bottom supporting bars [45] (see Fig. 1(d)).

At the Lea Lab, Mayes' 100 kN machine was used for punch tests. The die’s top radius must exceed the critical radius to provide an opening for DIC cameras, as in the macro-punch setup with 3D DIC. According to [47], the top-die diameter must satisfy the following equation (1)

$$A \geq D + 2t. \tag{1}$$

Eqn (1) was employed to minimize excessive specimen movement between the sample and the top die [44]. Accordingly, a curved chamfer consistent with macro-punch test configurations was adopted to reduce specimen shearing and ensure stable deformation [39,43], as shown in Fig. 1(a). The bottom die was mounted on the supporting bars of the testing machine (Fig. 1(d)), and an additional chamfer was introduced to improve specimen visibility and alignment for the 3D DIC system. Although the chamfer geometry influences the force–displacement response, the final design remains compliant with the criterion defined by Eq. (1). The large bottom die aperture ensured unobstructed imaging while maintaining specimen stability throughout the test.

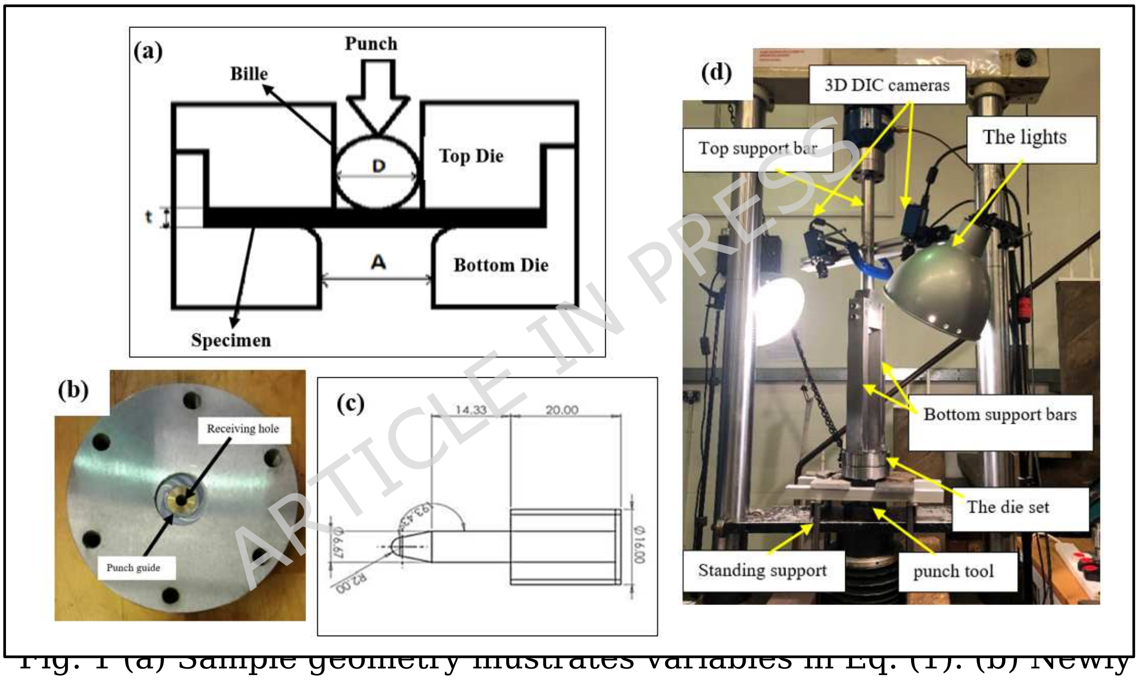

Fig. 1 (a) Sample geometry illustrates variables in Eq. (1). (b) Newly manufactured bottom die, and (c) Geometry of the punch in mm. (d) 3D DIC experiment setup with punch rig.

The bottom die was designed to securely constrain the specimen and provide sufficient rigidity to prevent twisting or deformation during loading, which could otherwise affect the force–displacement response [40], as illustrated in Fig. 1(b). A guided punch system was employed to ensure consistent punch specimen contact and accurate alignment, thereby improving test repeatability [16,45]. The punch geometry used in the present study is shown in Fig. 1(c). Overall, the punch die assembly enabled stable multiaxial loading and reliable force–displacement measurements while remaining fully compatible with full-field DIC observations and post-deformation microstructural analysis.

2.2. SP test procedure

2.2.1. SP test using 3D DIC

A circular disk with a diameter of 30 mm and a thickness of 1.5 mm was used as the specimen for the SP test. The design ensured compatibility with both the 3D DIC system and the SEM chamber. While the SP test follows the general principles of the macro-punch method, it was specifically adapted here for lab-scale formability assessment and detailed microstructural damage analysis in DP1000 steel. The specimen was first coated with a thin, uniform layer of white matte paint over its surface to ensure good adhesion throughout deformation. After drying, black spray paint was applied to create a randomly distributed speckle pattern, providing uniform coverage and sufficient contrast between the white background and black speckles for optimal DIC analysis. Special care was taken to maximize contrast and speckle sharpness, thereby enhancing strain resolution during DIC post-processing. The speckle size directly influences the achievable spatial resolution in DIC, as the subset size must be sufficiently large to contain multiple speckles to ensure reliable correlation. Smaller speckles permit the use of smaller subsets and thereby enhance spatial resolution; however, excessively small speckles increase measurement noise. An average speckle diameter of 3–7 pixels, therefore, provides an optimal compromise between spatial resolution and displacement accuracy. The displacement fields were calculated using a subset size of 31 pixels and a step size of 7 pixels, which offered a balanced trade-off between spatial resolution and strain noise [48-50].

The SP test rig was mounted on a 100 kN Mayes electromechanical testing machine (Fig. 1 (d)). The 3D DIC setup consisted of two high-resolution cameras mounted on a rigid support frame above the punch rig, connected to VIC-3D software (Correlated Solutions Inc.) for image acquisition and strain mapping. The camera positions were adjusted to focus on the central deformation zone of the specimen. Stereo calibration was performed using a dot-pattern calibration plate, which was systematically moved to introduce controlled combinations of in-plane rotation, out-of-plane tilt, and translational shifts [51, 52]. At least 25 calibration images were initially recorded, from which 15 high-quality images were selected to ensure the calibration error remained below 0.03. Upon successful calibration, the punch experiment was initiated, with synchronized image acquisition performed throughout the test to capture the evolving strain field and local deformation behavior up to specimen failure.

2.2.2. Validation of the SP test using FE modeling

To validate the SP test results, a FE simulation was conducted in Abaqus/Standard. The model geometry and boundary conditions replicated the experimental setup. Material behavior was defined using the true stress–strain curve of DP1000 steel obtained from uniaxial tensile tests, with a density of 7.85×10^{-6} kg/mm^3, Young's modulus of 180 GPa, and a Poisson's ratio of 0.3. The complete set of material properties implemented in the FE model, including tensile properties and the derived true stress–strain curve (see Appendix, Fig. A1), is summarized in Table 2. The specimen was modeled as an isotropic elastic–plastic circular disk (30 mm diameter, 1.5 mm thickness). The punch was defined as a rigid hemispherical body (2 mm radius); in contrast, dies were modeled as rigid surfaces. The specimen edge was fully constrained, and the punch displacement was restricted to 4 mm in the vertical (Y) direction under displacement control. Contact between the punch and specimen was modeled using a surface-to-surface penalty formulation with a friction coefficient of 0.35, determined from sensitivity analysis. The specimen was meshed using reduced integration linear hexahedral C3D8R elements, with local mesh refinement applied to the central deformation zone. The model consists of 12,736 elements and 14,401 nodes. Mesh sensitivity studies confirmed convergence and accurate strain gradient capture, with the adopted mesh strategy balancing computational efficiency and accuracy, as detailed in Section 3.2.1.

2.3. SP test using Inspect F SEM (without DIC)

The SP test provides a valuable method for investigating damage evolution under deformation conditions representative of practical forming operations. A custom-designed sample was developed to fit the stage of the Inspect F SEM (Fig. 2 and Fig. 3), allowing for periodic in-situ observation of microstructural damage throughout the test. Fig. 2 presents the sample geometry and the SEM holder, while Fig. 3 (b) shows the sample secured using two alignment pins. This configuration ensures precise repositioning after deformation, allowing consistent imaging of the same region.

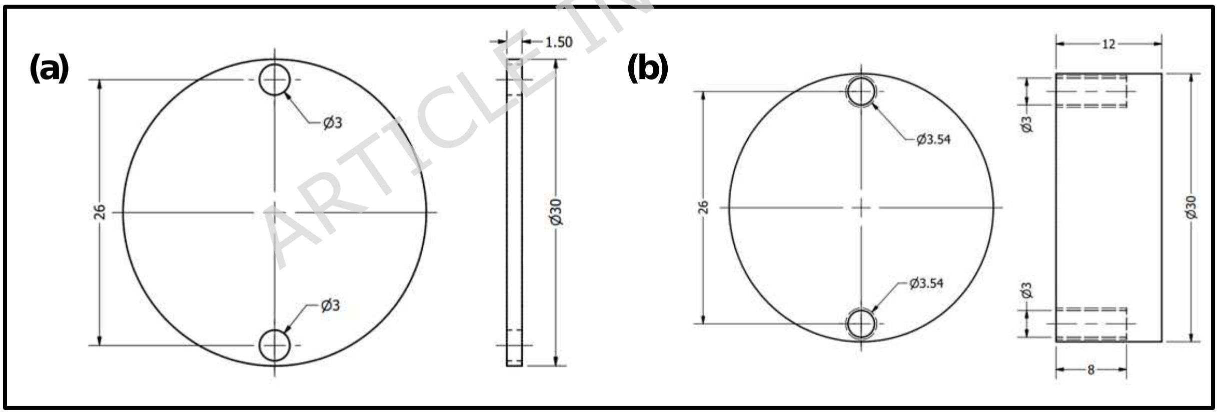

Fig. 2 (a) SP sample geometry (mm) and (b) SEM specimen-holder geometry in the Inspect F SEM (mm).

Before testing, the DP1000 steel sample was metallographically prepared to reveal its microstructure. The specimens were sequentially polished using SiC papers (P120, P400, P800, P1200) for 3–5 min each, followed by fine polishing with 6 µm and 1 µm diamond suspensions to achieve a mirror-like finish. The microstructure was revealed by etching in 2% nital for 4–12 s, with isopropanol cleaning between steps to avoid over-etching. Surface quality was verified using optical microscopy. The sample was mounted between the upper and lower dies using a locating key and six bolts. Deformation was applied using a punch tool through a die opening on a 100 kN electric Mayes machine (Lea Lab, University of Sheffield). The bottom die was supported by bars and blocks (refer to Fig. 3 (a), and the top die was fixed via overhead bars (see Fig. 3 (a)). The test was conducted in displacement-control mode at a rate of 1 mm/min, allowing interruption at any stage to observe early damage. SEM imaging of the undeformed sample was performed at various magnifications. The sample was then deformed to a 1 mm displacement and subsequently returned to the SEM for post-deformation analysis. This process was repeated until final failure.

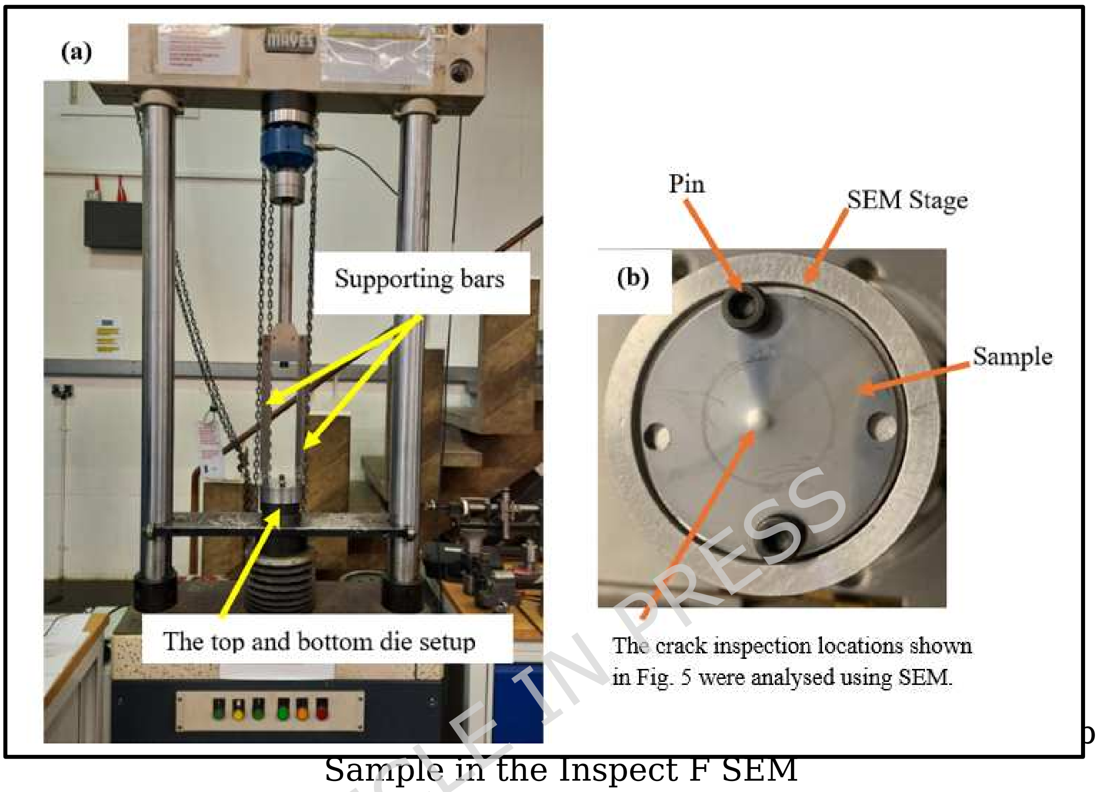

The crack inspection locations shown in Fig. 5 were analysed using SEM.

b)
Sample in the Inspect F SEM

3. Results and Discussion

The novel SP test developed in this study provided critical insights into microstructural damage evolution in DP1000 steel under biaxial loading conditions that closely mimic industrial forming processes. The results demonstrate that crack initiation and propagation in DP1000 steel are governed by a combined micromechanical interaction between F and M, rather than by a single phase acting independently. Damage initiates at the microstructural scale due to strain incompatibility and stress concentration at F–M interfaces, arising from the strong mechanical contrast between the soft F matrix and the hard M islands. The surrounding M imposes a significant constraint on F deformation, promoting localized plasticity, interfacial decohesion, and void nucleation within F ligaments. With continued loading, these voids grow and coalesce, while locally fractured or highly constrained M islands contribute to crack deflection and propagation, ultimately leading to specimen failure.

3.1 Load–Displacement Characteristics and SEM-Based Microstructural Damage Evolution

Fig.4 presents the load–displacement curve for the SP test, with imaging interruption points marked at displacements of 1.12 mm and 2.6 mm. The overall response illustrates the total displacement to failure. Consistent with previous studies [15, 52, 53], the curve can be divided into three characteristic regions: (I) elastic deformation, (II) plastic deformation, and (III) plastic flow accompanied by structural instability and fracture. Through-thickness surface crack propagation at the microstructural level was observed at the end of Region II and the onset of Region III, at a punch displacement of ~2.6 mm (Fig. 5), prior to the appearance of macroscopic surface cracks on the dome region. Early ferrite (F) damage and localized microstructural deformation were already detected in Region II at the first interruption point (1.12 mm). In Case 1, the crack shown in Fig. 5 likely initiated through the thickness before this displacement, whereas in Cases 2 and 3, crack initiation occurred near this value.[28, 30-32, 45].

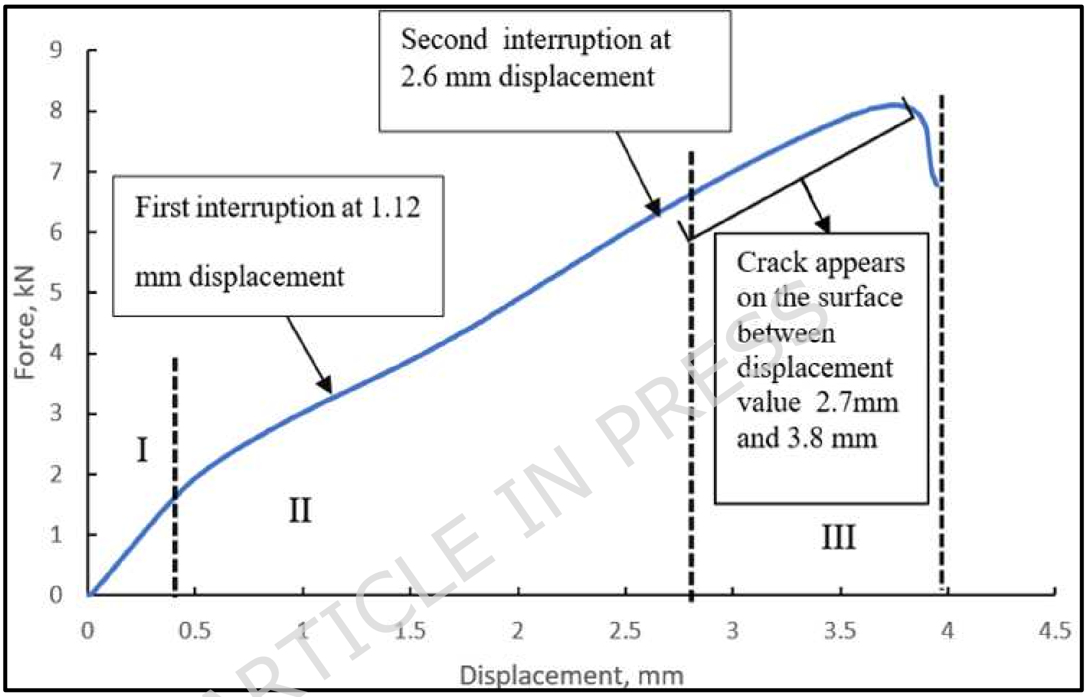

Fig. 4 Load-displacement curve with interruption points during SP test.

Fig. 5 presents representative SEM images from three different locations on the specimen surface during the SP test. At a punch displacement of 1.12 mm, small cracks were detected in the F matrix, (case 1, orange arrows in Fig. 5). In cases 1 also, 2 and 3, deformation was localized near the F-M interface (as indicated by the blue arrows in Fig. 5), leading to cracking of adjacent M islands (as shown by the red arrows in Fig. 5). These observations align with prior in-situ tensile test studies [31] [32]. The presence of cracks near the F-M interface plays a critical role in promoting M cracking in DP steel. Due to the strong mechanical contrast between the soft F matrix and the hard M phase, high strain localization and stress concentration develop at the interface during deformation. These localized stresses facilitate crack initiation at or near the interface, which can subsequently propagate into the brittle M islands. Consequently, localized M cracking occurs in regions adjacent to highly strained F, driven by stress concentrations at the F–M interface; however, this cracking acts in conjunction with F plastic deformation and interfacial decohesion rather than as an isolated failure mechanism. This interfacial effect highlights the importance of phase morphology and interfacial integrity in governing the fracture behaviour of dual-phase microstructures [23, 32, 39]. Further observations indicate that deformation bands localize within the F phase, resulting in shear band formation, microcracks in F, and fracture of adjacent M islands. This observation is consistent with [54], which reports that localized strain in the F phase of DP steels arises from the mechanical contrast with the harder M phase, leading to shear band formation and high strain gradients at F-M interfaces, promoting microcrack initiation in F and fracture of M islands.

The third column in Fig. 5 shows the microstructure after a punch displacement of 2.6 mm, where significant localized deformation and subsurface damage occurred without visible surface cracks. In Case 1, the crack propagated in the horizontal direction, whereas in Cases 2 and 3, cracks were oriented at approximately 45°. These orientations are attributed to microcracks in F located near adjacent M fractures and correspond to deformation along slip bands. Furthermore, the variation in crack propagation directions is governed by the combined effects of local microstructural heterogeneity and biaxial loading during the SP test [29, 55, 56]. Such behavior has also been highlighted in bending test observations [30]. The SP test proved highly effective for documenting microstructural damage evolution with high fidelity. SEM images of the specimen's top surface revealed early-stage M cracking (cases 2 and 3) and small F cracks at ~25% of the total displacement to failure (Fig. 4). M cracking observed here is consistent with tensile test results reported for DP1000 steel [31, 32]. However, this contrasts with the small F cracks previously reported in DP600 under uniaxial loading [37, 57, 58]. At this stage, cracks remained confined to individual F islands, highlighting the method's sensitivity to incipient damage.

The SP rig design enabled accurate specimen remounting after SEM imaging, allowing the test to continue uninterrupted by returning the specimen to the same position throughout the experiment. Subsequent interruptions revealed extensive microstructural crack propagation well before macroscopic fracture, consistent with prior findings in DP1000 [45]. Although large out-of-plane deformations limited detailed characterization at later stages (third column in Fig. 5), the overall trend of crack growth was still evident.

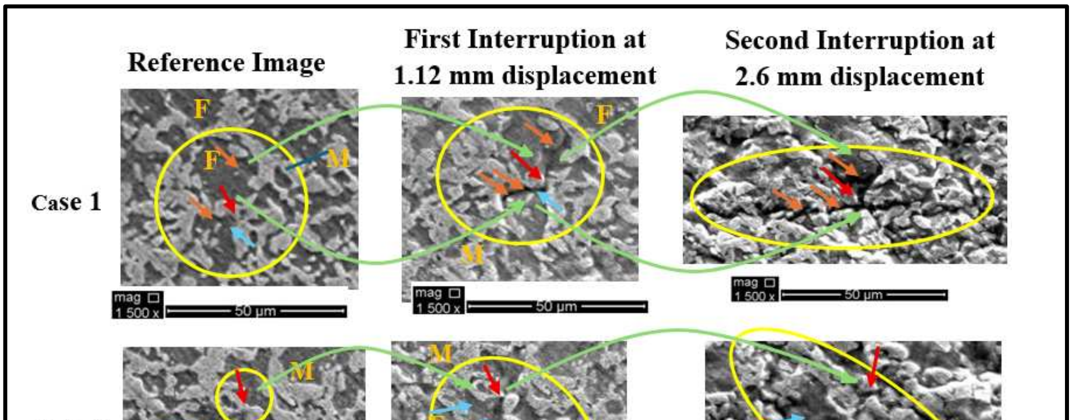

Fig. 5**.** Microstructural damage observed at three locations during the SEM SP test. Orange arrows (Case 1) indicate small F cracks, blue arrows (Cases 2 and 3) indicate deformation near the F–M interface, and red arrows indicate M fracture.

These results demonstrate that biaxial loading during the SP test accelerates crack propagation, in line with [45], but not clearly captured in tensile tests of DP1000 [31, 32]. The formation of microcracks between 1.12 mm and 2.6 mm (region II, Fig. 4) underscores the capability of the SP test to capture progressive microstructural damage leading to fracture in DP1000 steel. Collectively, these findings validate the SP methodology as a robust approach for in-situ characterization of damage mechanisms under forming-like deformation conditions.

3.2 Crack Analysis of SP Test Sample Measured Using DIC

3.2.1 Strain Distribution Measurement using DIC

A new rig incorporating 3D DIC was designed and manufactured for the SP test (Section 2) [60 ,59] . Cameras were positioned to capture full-field deformation, and strain distributions were processed using Correlated Solutions VIC-3D software. The evolution of out-of-plane displacement in the Z-direction is shown in Fig. 6, with a maximum surface displacement of 2.59 mm before and after sample failure (Figs. 6(a) and 6(b)). The machine-applied punch displacement exceeded the DIC-measured surface displacement by approximately 1.4 mm, as DIC captures only surface deformation rather than through-thickness motion. The maximum principal strain (Exx) on the specimen surface just before crack observation is shown in Fig. 8.

The first surface-visible crack appeared in a region where Exx ≈ 0.17, which is below the global maximum. This atypical crack location is likely influenced by the strong constraint and high-contact stress state beneath the punch, conditions that are further affected by an elevated effective coefficient of friction between the punch and specimen surface (μ = 0.35), as identified in FE sensitivity analysis. These effects are further visualized through strain evolution plots in Appendix A (Fig. A2), where early localized strain development beneath the punch precedes the region of maximum strain. As the load increased, the strain progressively localized toward the specimen center, reaching Exx ≈ 0.234 immediately before the surface crack became visible (Fig. 8). This localization trend and crack formation mechanism are consistent with earlier studies on dual-phase steels from Erichsen cupping tests, where fractures in DP600 and DP780 were typically observed near the dome apex and oriented parallel to the rolling direction [39, 53, 54], although the SP geometry and constrained contact evolution in this work result in a more localized deformation field.

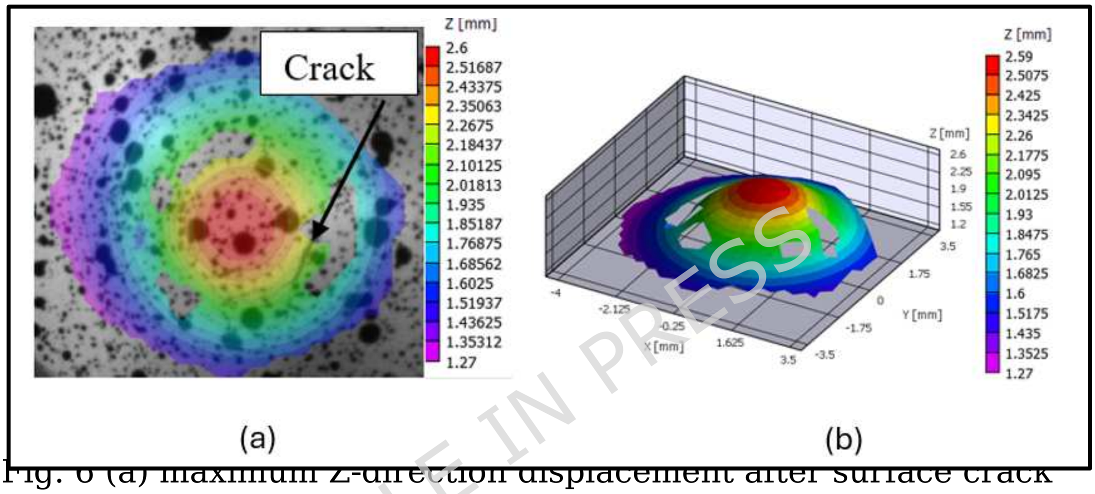

Fig. 6 (a) maximum Z-direction displacement after surface crack appearance; (b) 3D DIC out-of-plane displacement before crack appearance.

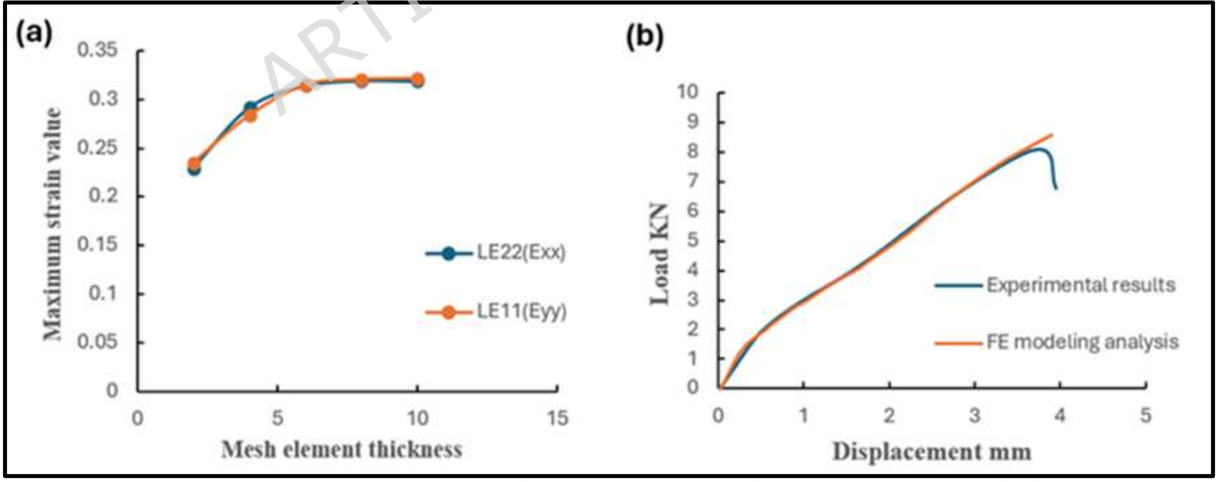

Fig. 7 (a) Maximum Exx and Eyy strain values for SP model mesh element sizes 2, 4, 6, and 8. (b) Comparison of experimental and modeled load-displacement curves for the SP test.

FE simulations were performed to validate experimental observations, following methodologies from previous studies [30, 31, 61-63]. A mesh-refinement study based on the Exx and Eyy strain values, using through-thickness element sizes of 2, 4, 6, and 8 μm (Fig. 7(a)), demonstrated that an 8 µm element size provides mesh-independent results while maintaining computational efficiency. The FE-predicted load-displacement response (excluding damage modeling) closely matched experimental results up to the maximum load (Fig. 7(b)), in agreement with previous simulation and experimental correlations reported for Grade 91 steel [15]. For DP1000, the maximum punch force was approximately 8 kN, with failure displacement of 4 mm. In comparison, macro-scale tests such as the Erichsen Cup and Hole Expansion tests for DP600 and DP780 exhibit higher maximum punch forces and larger or smaller displacements depending on alloy and test type [64]. Therefore, the SP test successfully facilitated the progressive development of damage in DP1000 up to the point of failure. Additionally, the integration of 3D DIC with the punch test provided detailed, full-field information on surface deformation, consistent with observations reported in [30, 31, 45, 60, 65].

To better capture deformation evolution during the SP test, surface strain was analyzed over the full punch displacement history. Representative Exx strain contours at selected deformation stages, from initial contact to just before surface crack appearance, are presented in Appendix A (Fig. A3), illustrating the progressive intensification and localization of strain beneath the punch. The maximum local surface strain was further correlated with the imposed punch displacement (Appendix A, Fig. A4), providing a quantitative link between displacement, strain localization, and damage evolution. Corresponding interrupted tests were examined by SEM, enabling direct correlation of strain evolution with microstructural damage.

Fig. 8 compares FE-predicted strain distributions (LE11) with DIC measurements (Exx), demonstrating good agreement and confirming that the model captures plastic deformation accurately before fracture. The first surface-visible crack appeared at a local Exx of ~23.8%, lower than the ~50% reported in macro-punch tests [45], highlighting the SP test's sensitivity to early microstructural damage. This difference is primarily attributed to the reduced sample geometry, different damage propagation process, and the associated change in stress state rather than to the experimental setup itself. Compared to macroscopic tests, the thin SP specimens experience higher stress triaxiality, steeper through-thickness strain gradients, and stronger constraint effects, all of which promote earlier crack initiation at lower global strain levels. Similar thickness and stress-state-dependent effects on damage initiation have been reported in formability and fracture studies of advanced high-strength steels [30-32].

Unlike uniaxial tensile testing, biaxial loading better represents the complex strain paths encountered during forming operations. This approach more accurately reflects the conditions in many industrial forming processes than simple uniaxial stretching, as demonstrated in previous studies [45, 60, 64, 66], which employed similar methodologies. In this study, 3D DIC was integrated with the punch test to evaluate the formability of AHSS. The resulting strain distributions were highly non-uniform, exhibiting pronounced strain localization (necking) and elevated strain levels in specific regions. Furthermore, this methodology enabled detailed tracking of strain path evolution, providing critical insights into the material’s forming limits.

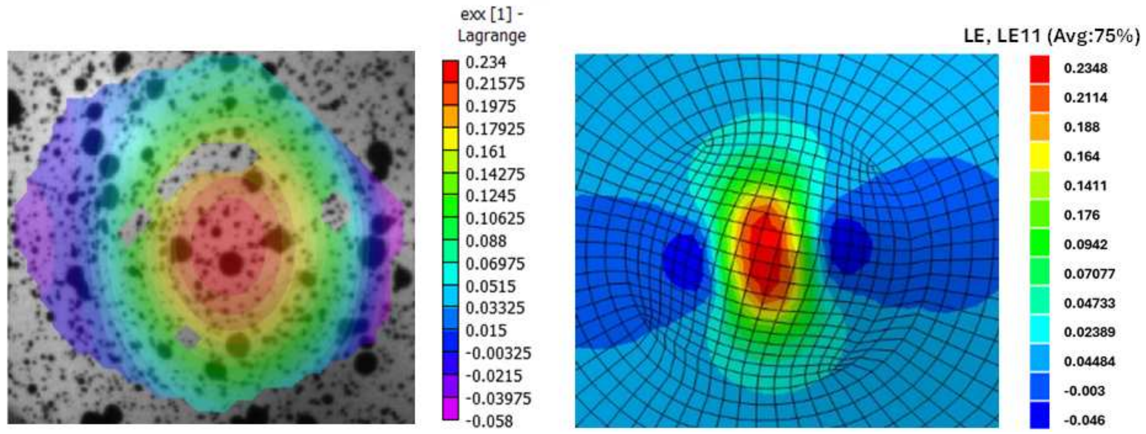

Fig. 8 LE11 strain distribution from Abaqus vs. experimental 3D DIC E_{xx} strain distribution of the SP test before crack observe at the sample surface.

In macro-punch tests reported by Rohaizat et al. [45], crack initiation was observed at either the top surface or the tool-contact surface, whereas in the present SP tests, crack initiation consistently occurred at the tool-contact surface, reflecting differences in contact conditions and stress gradients inherent to thinner specimens. Moreover, the localized deformation captured via DIC in the SP test revealed a broader strain range associated with M cracking compared to macro-scale measurements. When compared with conventional uniaxial tensile DIC tests, where maximum strains of ~14% have been reported for DP1000 [45, 67], the higher local strain measured here further highlights the influence of multiaxial stress state, out-of-plane deformation, and severe strain localization beneath the punch. These results demonstrate that the SP–DIC approach captures localized deformation and damage mechanisms that are not accessible through conventional macroscopic formability tests.

3.2.2 Crack Propagation Analysis

Crack development in the damaged region of the SP test specimen, tracked via DIC, was investigated through cross-sectional analysis. Before sectioning, the DIC paint and speckle pattern were removed, and the surface was prepared for cutting. A 5 mm × 5 mm area surrounding the damage site was excised using a Secotom-50 cutting machine. The specimen was then bisected along its centerline and mounted in conductive Bakelite (Fig. 9). Following grinding, polishing, and etching, the cross-section was examined using the Inspect F SEM.

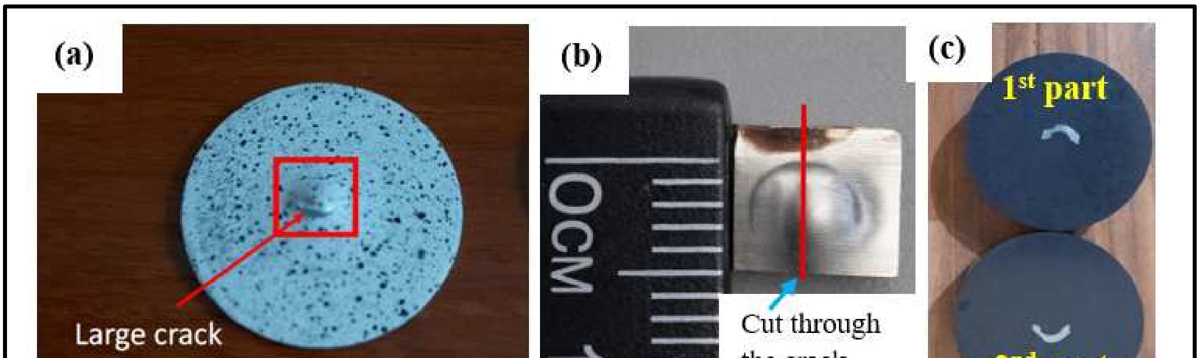

Fig. 9(a) Area cut around the crack; (b) second cut through the crack; (c) samples mounted for SEM observation.

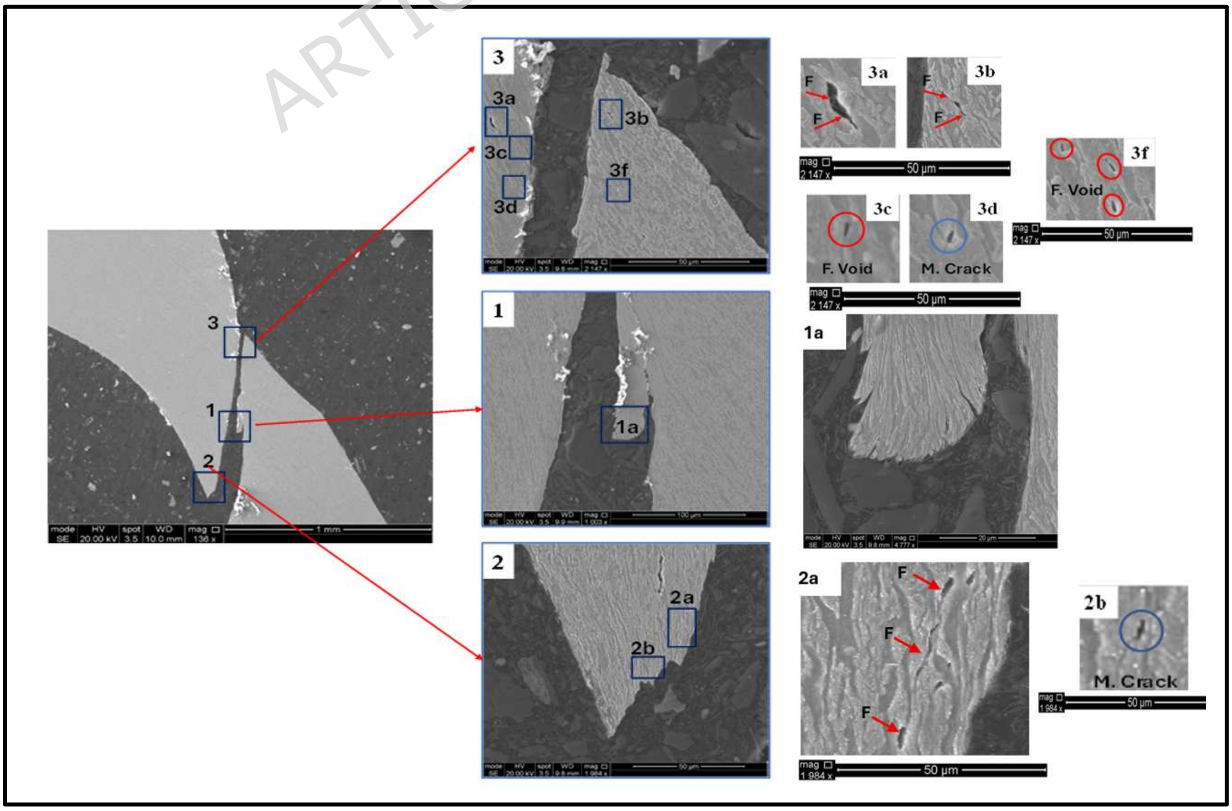

Fig. 10**.** Cross-sectional SEM micrographs showing crack-propagation features in the first region of the SP test specimen after DIC-monitored fracture.

Fig. 10 presents the cross-sectional microstructure of the DIC-SP test specimen. In the mid-thickness region, secondary cracks branched from the primary crack (region 1). A secondary crack in region 1a predominantly traversed the F, winding around highly deformed M islands, consistent with observations reported in [45]. M cracks were observed in regions 2b and 3d (Fig. 10) and 4b-3 and 5a (Fig. 11). Additionally, a decohesion of F-M interface and crack propagation through F phase were observed below the surface in regions 2a and 3b (Fig. 10) and 4a-1 and 4b-1 (Fig. 11), while F voids were identified in regions 3c and 3f (Fig. 10). These observations confirm that crack propagation in DP1000 during the final damage stage results from interfacial decohesion and F void coalescence following extensive F deformation under the mechanical constraint imposed by surrounding M, with locally fractured M islands influencing crack path deflection and progression [23, 24, 30, 58]. Cracks in the F matrix of DP steels significantly influence the material's overall mechanical behaviour and fracture progression. F, being the softer and more ductile phase, typically accommodates plastic deformation during loading. However, when cracks initiate or propagate within the F matrix, they act as stress concentrators and reduce the load-bearing capacity of the surrounding material. These cracks can also interact with neighbouring M islands, enhancing local stress concentrations at the F-M interface. Consequently, crack growth in F can accelerate M cracking and lead to void coalescence, promoting overall failure. The morphology, distribution, and connectivity of these cracks critically determine the fracture toughness and ductility of DP steels [30, 68, 69]. The widest opening along the primary crack indicates initiation at the surface in contact with the punch, propagation through the full thickness, and emergence at the upper surface, where strains were captured via DIC (Section 3.2.1).

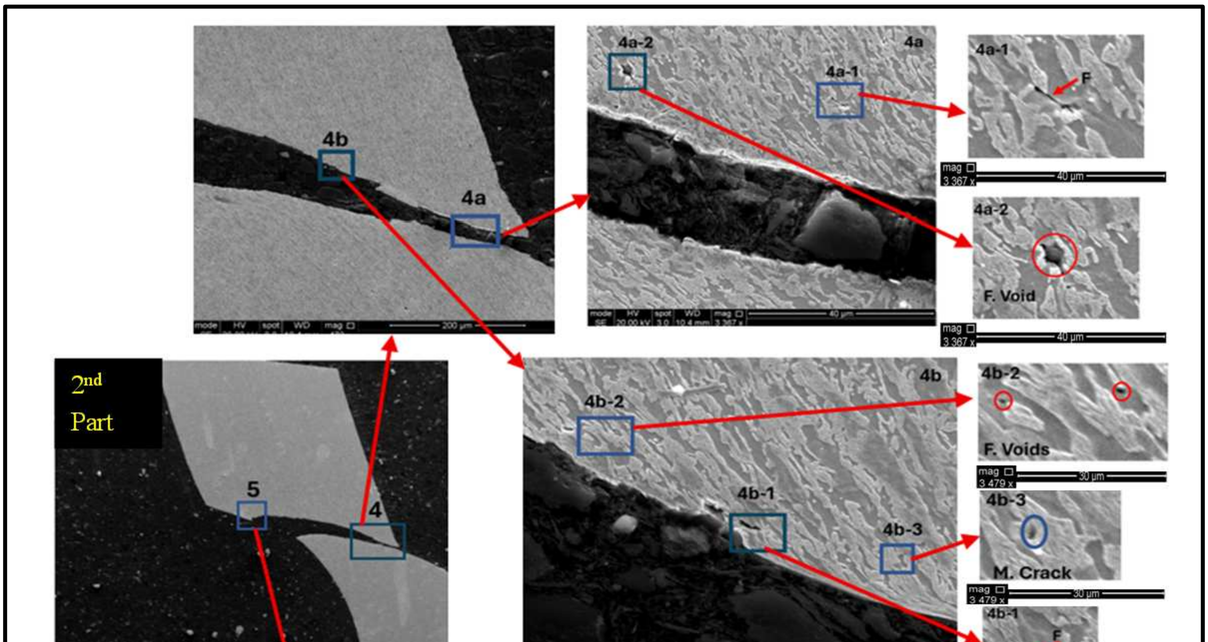

Fig. 11. SEM observation of crack features in the second region of the SP test specimen after the 3D DIC sample fractured through the thickness.

Cross-sectional SEM analysis (Figs. 10 and 11) elucidated the dominant damage mechanisms leading to failure. Multiple large voids and secondary cracks were predominantly located within the F phase and developed after significant microstructural deformation. These voids preferentially nucleated near F-M interfaces, consistent with F acting as the primary damage initiation [70] site, as reported in [29, 57, 71]. Cracks then propagated along phase boundaries or through elongated M islands when their orientation favored fracture progression. The primary crack path originated at the tool-contact surface and traversed fragmented M islands, highlighting the complex interaction between microstructural constituents during crack propagation. The early-stage dominance of M cracking in DP1000 corroborates prior findings [31, 32] and aligns with observations in other dual-phase steels [37, 57, 58]. Typically, cracks initiating within M islands propagated locally but arrested at F-M interfaces, reflecting mechanical mismatch and crack blunting effects at phase boundaries, consistent with observations in [24, 37, 58, 72]. While macro punch tests documented crack propagation in DP1000 [45], such features were absent in in-situ SEM tensile investigations [30-32, 45].

The SP test methodology combining periodic interruption with SEM imaging enabled detailed observation of microstructural damage initiation and propagation in DP1000 steel, consistent with earlier reports on dual-phase steels [24, 26, 27, 39, 65]. Early-stage F cracking was captured during interrupted stages, offering temporal insight into the onset and progression of damage. However, because deformation was applied in relatively large increments between interruptions, the spatial resolution of strain evolution at the microstructural scale could not be continuously monitored. In addition, the inherently two-dimensional nature of SEM limits direct visualization of subsurface crack networks and void connectivity, despite the ability to correlate damage evolution with surface strain localization using interrupted SEM and DIC. Nevertheless, the dominant damage mechanisms remain clearly identifiable. Cross-sectional inspections confirmed that cracks propagated primarily through the ferrite matrix, with occasional traversal of martensite islands depending on their morphology, alignment, and associated stress concentrations, highlighting the essential influence of microstructural heterogeneity on damage localization and failure in DP1000 steel. Future application of advanced three-dimensional characterization techniques, such as X-ray computed tomography, would help overcome these limitations by enabling full 3D reconstruction of damage evolution.

While the present study effectively links damage evolution to surface strain localization using interrupted SEM and DIC, the inherently two-dimensional nature of SEM restricts visualization of subsurface crack networks and void connectivity. Advanced three-dimensional imaging techniques, such as X-ray computed tomography, would help resolve these limitations and enable a full 3D reconstruction of damage. Moreover, the present experimental findings establish a foundation for microstructure-based multiscale modeling, providing critical input for predictive tools aimed at forecasting deformability and damage evolution in dual-phase steels under complex loading conditions.

4. Conclusion

A novel SP test integrating 3D DIC was developed to investigate microstructural damage evolution in DP1000 steel under biaxial loading conditions representative of industrial forming processes. This innovative approach enabled direct observation of damage initiation and propagation at the microscale by periodically interrupting the test and transferring specimens between the test rig and SEM. Microstructural crack initiation could not be captured due to the intermittent nature of SEM imaging; nevertheless, damage was observed in both F and M, often concentrated near F-M interfaces, with F void formation and M cracking progressing through significant plastic deformation up to final failure, indicating that these mechanisms dominate the fracture process of DP1000 under the tested conditions. Macroscopic 3D DIC strain measurements indicated a surface-crack strain of approximately 23%, consistent with the observed microscale damage evolution. Compared to lower-strength dual-phase steels, the damage evolution in DP1000 appears more progressive, suggesting a prolonged void nucleation and coalescence process prior to macroscopic cracking. This behavior is attributed to the fine ferrite grain size and Nb microalloying in DP1000, which are expected to reduce strain gradients between ferrite and martensite, enhance local deformation compatibility, and delay damage localization at phase interfaces. Cross-sectional SEM analyses further elucidated the damage mechanisms, revealing that crack propagation predominantly occurred through F regions and occasionally traversed M islands aligned along the crack path. Additionally, SP testing reveals microstructural damage features that differ from those observed under uniaxial tension, emphasizing the influence of multiaxial stress states on void nucleation and crack propagation. This comprehensive multi-scale experimental methodology provides valuable insights into the complex damage progression of DP steels.

Key conclusions from this work include:

- The SP test combined with 3D DIC offers a robust technique to study microstructural damage under biaxial loading with the ability to interrupt and observe damage evolution via SEM.
- Damage observed after test interruption occurred in both F and M, often near F-M interfaces; however, the precise initiation event could not be directly resolved with the current methodology.
- The F phase accommodates the majority of plastic deformation before void formation; however, damage progression and final failure are governed by the interaction between F plasticity, martensitic constraint, and strain incompatibility at F–M interfaces, and microstructural refinement associated with Nb microalloying, rather than by F behavior alone.
- The surface-crack strain (~23%) measured by 3D DIC is lower than that reported in conventional macro-scale punch tests, highlighting the influence of test geometry, constraint effects, and damage evolution mechanisms.

This study lays the groundwork for future efforts integrating experimental and modeling approaches to advance the understanding and prediction of damage evolution in advanced high-strength steels under complex loading.

Acknowledgements

The first author conducted all experiments at the laboratories of The University of Sheffield, Mappin Street, Sheffield S1 3JD, UK. The authors gratefully acknowledge Tata Steel Europe, IJmuiden, the Netherlands, for providing the materials essential to this research.
This scientific paper was derived from a research grant funded by Taibah University, Madinah, Kingdom of Saudi Arabia – with Grant Number (447-13-1054).

Data availability statement

The experimental datasets obtained from this research work and the analysed results during the current study are available from the corresponding author on reasonable request.

Declaration of Competing Interest

The authors declare that they have no known competing financial interests or personal relationships.

Funding

This work was funded by Taibah University, Madinah, Kingdom of Saudi Arabia with grant number (447-13-1054).

CRediT authorship contribution statement

Asim Alsharif: Writing – original draft, Visualization, Project administration, Methodology, Validation, Investigation, Formal analysis, Conceptualization, Funding acquisition, Data collection. **Syed Quadir Moinuddin:** Writing – review & editing, Writing – original draft, Validation, Project administration, Investigation. **Christophe Pinna:** Writing – review & editing, Validation, Supervision, Resources, Methodology, Investigation, Conceptualization.

References

1. Hou, Y., et al., *A review of characterization and modelling approaches for sheet metal forming of lightweight metallic materials.* Materials, 2023. **16**(2): p. 836.
2. Dixit, U.S., *Modeling of metal forming: a review.* Mechanics of materials in modern manufacturing methods and processing techniques, 2020: p. 1–30.
3. Lesch, C., N. Kwiaton, and F.B. Klose, *Advanced high strength steels (AHSS) for automotive applications− tailored properties by smart microstructural adjustments.* steel research international, 2017. **88**(10): p. 1700210.
4. Liu, Y., et al., *Ductile fracture of dual-phase steel sheets under bending.* International Journal of Plasticity, 2020. **125**: p. 80–96.
5. Hosford, W.F. and R.M. Caddell, *Metal forming: mechanics and metallurgy.* 2011: Cambridge university press.
6. ISO, D., *Metallic materials-Sheet and strip-Determination of forming-limit curves-Part 2: Determination of forming-limit curves in the laboratory.* ISO, 2008.
7. Yoon, J.-H., et al., *Earing predictions for strongly textured aluminum sheets.* International journal of mechanical sciences, 2010. **52**(12): p. 1563–1578.
8. ASTM, *E643 -15 Standard Test Method for Ball Punch Deformation of Metallic Sheet Material.* ASTM, 2015: p. 4.
9. Mendes-Fonseca, N., et al., *A comparative study on the bendability of a Dual Phase steel: Three-point bend versus V-die test.* Journal of Materials Research and Technology, 2025.
10. Paul, S.K., et al., *Identification of post-necking tensile stress–strain behavior of steel sheet: An experimental investigation using digital image correlation technique.* Journal of Materials Engineering and Performance, 2018. **27**(11): p. 5736–5743.
11. Paul, S.K., *Effect of microstructure and deformation mechanisms on the forming limit curve of automotive steels and aluminium alloys.* International Journal of Lightweight Materials and Manufacture, 2025.
12. Paul, S.K., *Controlling factors of forming limit curve: A review.* Advances in Industrial and Manufacturing Engineering, 2021. **2**: p. 100033.
13. Paul, S.K., *A critical review on hole expansion ratio.* Materialia, 2020. **9**: p. 100566.
14. Kamikawa, N. and H. Morino, *Quantitative Analysis of Load–Displacement Curves in Erichsen Cupping Test for Low Carbon Steel Sheet.* Metallurgical and Materials Transactions A, 2019. **50**(11): p. 5023–5037.
15. Simonovski, I., S. Holmström, and M. Bruchhausen, *Small punch tensile testing of curved specimens: Finite element analysis and experiment.* International Journal of Mechanical Sciences, 2017. **120**: p. 204–213.
16. Mao, X., M. Saito, and H. Takahashi, *Small punch test to predict ductile fracture toughness JIC and brittle fracture toughness KIC.* Scripta Metallurgica et Materialia, 1991. **25**(11): p. 2481–2485.
17. Foulds, J.R., et al., *Fracture toughness by small punch testing.* Journal of testing and evaluation, 1995. **23**(1): p. 3–10.
18. Milička, K. and F. Dobeš, *Small punch testing of P91 steel.* International Journal of Pressure Vessels and Piping, 2006. **83**(9): p. 625–634.
19. Budzakoska, E., et al., *Predicting the J integral fracture toughness of Al 6061 using the small punch test.* Fatigue & Fracture of Engineering Materials & Structures, 2007. **30**(9): p. 796–807.

20. Mao, X. and H. Takahashi, *Development of a further-miniaturized specimen of 3 mm diameter for tem disk (ø 3 mm) small punch tests.* Journal of Nuclear Materials, 1987. **150**(1): p. 42–52.
21. Rodríguez, C., et al., *Fracture characterization of steels by means of the small punch test.* Experimental Mechanics, 2013. **53**(3): p. 385–392.
22. Peng, Y.-Q., et al., *Determination of the tensile and fracture properties of ductile materials by small punch testing.* Journal of Nuclear Science and Technology, 2021. **58**(7): p. 735–743.
23. Avramovic-Cingara, G., et al., *Effect of martensite distribution on damage behaviour in DP600 dual phase steels.* Materials Science and Engineering: A, 2009. **516**(1): p. 7–16.
24. Saeidi, N., et al., *Damage mechanism and modeling of void nucleation process in a ferrite–martensite dual phase steel.* Engineering Fracture Mechanics, 2014. **127**: p. 97–103.
25. Peng, Y.Q., et al., *A Novel Method to Predict the Mechanical Properties of DP600.* Key Engineering Materials, 2019. **795**: p. 22–28.
26. Alaie, A., et al., *Effect of microstructure pattern on the strain localization in DP600 steels analyzed using combined in-situ experimental test and numerical simulation.* Materials Science and Engineering: A, 2015. **638**: p. 251–261.
27. Kadkhodapour, J., A. Butz, and S.Z. Rad, *Mechanisms of void formation during tensile testing in a commercial, dual-phase steel.* Acta Materialia, 2011. **59**(7): p. 2575–2588.
28. Ososkov, Y., et al., *In-situ measurement of local strain partitioning in a commercial dual-phase steel.* International Journal of Materials Research, 2007. **98**(8): p. 664–673.
29. Ghadbeigi, H., C. Pinna, and S. Celotto, *Failure mechanisms in DP600 steel: initiation, evolution and fracture.* Materials Science and Engineering: A, 2013. **588**: p. 420–431.
30. Alsharif, A., et al., *In-Situ microstructure characterization and micromechanical modelling of damage initiation and propagation in DP1000 dual phase steel.* Materials & Design, 2025: p. 114684.
31. Alharbi, K., et al., *Damage in dual phase steel DP1000 investigated using digital image correlation and microstructure simulation.* Modelling and Simulation in Materials Science and Engineering, 2015. **23**(8): p. 085005.
32. Ghadbeigi, H., et al., *Local plastic strain evolution in a high strength dual-phase steel.* Materials Science and Engineering: A, 2010. **527**(18-19): p. 5026–5032.
33. Soyarslan, C., M.M. Gharbi, and A. Tekkaya, *A combined experimental–numerical investigation of ductile fracture in bending of a class of ferritic–martensitic steel.* International Journal of Solids and Structures, 2012. **49**(13): p. 1608–1626.
34. Reche, D., et al., *Damage development in low alloy TRIP-aided steels during air-bending.* Materials Science and Engineering: A, 2011. **528**(15): p. 5241–5250.
35. Wang, W. and X. Wei, *The effect of martensite volume and distribution on shear fracture propagation of 600–1000 MPa dual phase sheet steels in the process of deep drawing.* International Journal of Mechanical Sciences, 2013. **67**: p. 100–107.
36. Uthaisangsuk, V., U. Prahl, and W. Bleck, *Characterisation of formability behaviour of multiphase steels by micromechanical modelling.* International Journal of Fracture, 2009. **157**(1): p. 55–69.
37. Avramovic-Cingara, G., et al., *Effect of martensite distribution on damage behaviour in DP600 dual phase steels.* Materials Science and Engineering: A, 2009. **516**(1-2): p. 7–16.
38. Pelligra, C., et al., *The effect of vanadium on microstrain partitioning and localized damage during deformation of unnotched and notched DP1300 steels.* International Journal of Plasticity, 2022. **158**: p. 103435.
39. Tasan, C.C., et al., *Integrated experimental–simulation analysis of stress and strain partitioning in multiphase alloys.* Acta Materialia, 2014. **81**: p. 386–400.
40. Tasan, C.C., et al., *Strain localization and damage in dual phase steels investigated by coupled in-situ deformation experiments and crystal plasticity simulations.* International Journal of Plasticity, 2014. **63**: p. 198–210.

41. Basu, S., et al., *Study of microstructure-property correlations in dual phase steels for achieving enhanced strength and reduced strain partitioning.* Materialia, 2022. **25**: p. 101522.
42. Basu, S., et al., *Size and microstructural factors affecting the micro-hole expansion ratio and fracture toughness of dual phase steel sheets.* Materials Science and Engineering: A, 2025. **919**: p. 147517.
43. Tasan, C.C., et al., *An overview of dual-phase steels: advances in microstructure-oriented processing and micromechanically guided design.* Annual Review of Materials Research, 2015. **45**: p. 391–431.
44. Rashid, M., *Dual phase steels.* Annual Review of Materials Science, 1981. **11**(1): p. 245–266.
45. Rohaizat, N.I., *Fracture of automotive high strength steels*. 2018, University of Sheffield.
46. Altstadt, E., et al., *Critical evaluation of the small punch test as a screening procedure for mechanical properties.* Journal of Nuclear Materials, 2016. **472**: p. 186–195.
47. Habibi, S., A. Ziadi, and A. Megueni, *Modeling a Small Punch Testing Device.* Engineering, Technology & Applied Science Research, 2014. **4**(2): p. 612–617.
48. Sutton, M.A., J.J. Orteu, and H. Schreier, *Image correlation for shape, motion and deformation measurements: basic concepts, theory and applications*. 2009: Springer Science & Business Media.
49. Pan, B., et al., *Two-dimensional digital image correlation for in-plane displacement and strain measurement: a review.* Measurement science and technology, 2009. **20**(6): p. 062001.
50. Reu, P., *All about speckles: speckle size measurement.* Experimental Techniques, 2014. **38**(6): p. 1–2.
51. Lobanov, D. and E. Strungar, *Mathematical data processing according to digital image correlation method for polymer composites.* Fracture and Structural Integrity, 2020. **14**(54): p. 56–65.
52. Martínez-Pañeda, E., et al., *Damage modeling in small punch test specimens.* Theoretical and applied fracture mechanics, 2016. **86**: p. 51–60.
53. Abendroth, M. and M. Kuna, *Determination of deformation and failure properties of ductile materials by means of the small punch test and neural networks.* computational materials Science, 2003. **28**(3-4): p. 633–644.
54. Park, M.-h., et al., *Grain size effects on strain localization and fracture behavior in ferrite–martensite dual-phase steels characterized by digital image correlation analysis.* Journal of Materials Research and Technology, 2025.
55. Liu, L., et al., *An integrated experimental-numerical study of martensite/ferrite interface damage initiation in dual-phase steels.* Scripta Materialia, 2024. **239**: p. 115798.
56. Tian, C. and C. Kirchlechner, *The fracture toughness of martensite islands in dual-phase DP800 steel.* Journal of Materials Research, 2021. **36**(12): p. 2495–2504.
57. Calcagnotto, M., et al., *Deformation and fracture mechanisms in fine-and ultrafine-grained ferrite/martensite dual-phase steels and the effect of aging.* Acta Materialia, 2011. **59**(2): p. 658–670.
58. Erdogan, M., *The effect of new ferrite content on the tensile fracture behaviour of dual phase steels.* Journal of Materials Science, 2002. **37**: p. 3623–3630.
59. Hammer, J.T., et al., *Using Digital Image Correlation (DIC) in Dynamic Punch Tests.* Experimental Mechanics, 2014. **55**(1): p. 201–210.
60. Chen, X., et al., *Full Field Strain Measurement of Punch-stretch Tests Using Digital Image Correlation.* SAE International Journal of Materials and Manufacturing, 2012. **5**(2): p. 345–351.
61. Ha, J., et al., *Investigation of plastic strain rate under strain path changes in dual-phase steel using microstructure-based modeling.* International Journal of Plasticity, 2017. **93**: p. 89–111.
62. Gothivarekar, S., et al., *Advanced FE model validation of cold-forming process using DIC: Air bending of high strength steel.* International Journal of Material Forming, 2020. **13**(3): p. 409–421.

63. Ridwan, R., et al., *Tensile analysis and assessment of carbon and alloy steels using fe approach as an idealization of material fractures under collision and grounding.* Curved and Layered Structures, 2020. **7**(1): p. 188–198.
64. Santos, R.O., et al., *Development of a Device Compatible with Universal Testing Machine to Perform Hole Expansion and Erichsen Cupping Tests.* Machines, 2020. **8**(1): p. 2.
65. Ghadbeigi, H., C. Pinna, and S. Celotto, *Quantitative strain analysis of the large deformation at the scale of microstructure: comparison between digital image correlation and microgrid techniques.* Experimental mechanics, 2012. **52**: p. 1483–1492.
66. Fathi, H., et al., *Effect of punch speed on the formability behavior of austenitic stainless steel type 304L.* "Metals and Materials International", 2016. **22**(3): p. 397–406.
67. Alharbi, K., *Damage Investigation in Dual-Phase 1000 Steel and Behaviour Prediction Using Microstructure Based Modelling*. 2015, University of Sheffield.
68. Sun, X., et al., *On key factors influencing ductile fractures of dual phase (DP) steels.* Materials Science and Engineering: A, 2009. **526**(1): p. 140–149.
69. Asik, E.E., *Damage in dual phase steels.* 2019.
70. Alaie, A., et al., *Formation and coalescence of strain localized regions in ferrite phase of DP600 steels under uniaxial tensile deformation.* Materials Science and Engineering: A, 2015. **623**: p. 133–144.
71. Calcagnotto, M., D. Ponge, and D. Raabe, *Effect of grain refinement to 1 μm on strength and toughness of dual-phase steels.* Materials Science and Engineering: A, 2010. **527**(29-30): p. 7832–7840.
72. Avramovic-Cingara, G., et al., *Void nucleation and growth in dual-phase steel 600 during uniaxial tensile testing.* Metallurgical and Materials Transactions A, 2009. **40**(13): p. 3117.